

## High-Q inverted silica microtoroid resonators monolithically integrated into a silicon photonics platform

Richter, Jens; Nezhad, Maziar P.; Hadam, Birgit; Taubner, Thomas; Knoch, Joachim; Merget, Florian; Moscoso-Mártir, Alvaro; Witzens, Jeremy

### Optics Express

DOI:  
[10.1364/OE.26.027418](https://doi.org/10.1364/OE.26.027418)

Published: 15/10/2018

Publisher's PDF, also known as Version of record

[Cyswllt i'r cyhoeddiad / Link to publication](#)

*Dyfyniad o'r fersiwn a gyhoeddwyd / Citation for published version (APA):*  
Richter, J., Nezhad, M. P., Hadam, B., Taubner, T., Knoch, J., Merget, F., Moscoso-Mártir, A., & Witzens, J. (2018). High-Q inverted silica microtoroid resonators monolithically integrated into a silicon photonics platform. *Optics Express*, 26(21), 27418-27440.  
<https://doi.org/10.1364/OE.26.027418>

#### Hawliau Cyffredinol / General rights

Copyright and moral rights for the publications made accessible in the public portal are retained by the authors and/or other copyright owners and it is a condition of accessing publications that users recognise and abide by the legal requirements associated with these rights.

- Users may download and print one copy of any publication from the public portal for the purpose of private study or research.
- You may not further distribute the material or use it for any profit-making activity or commercial gain
- You may freely distribute the URL identifying the publication in the public portal ?

#### Take down policy

If you believe that this document breaches copyright please contact us providing details, and we will remove access to the work immediately and investigate your claim.



# High-Q inverted silica microtoroid resonators monolithically integrated into a silicon photonics platform

JENS RICHTER,<sup>1</sup> MAZIAR P. NEZHAD,<sup>1,2</sup> BIRGIT HADAM,<sup>3</sup> THOMAS TAUBNER,<sup>4</sup> JOACHIM KNOCH,<sup>3</sup> FLORIAN MERGET,<sup>1</sup> ALVARO MOSCOSO-MÁRTIR,<sup>1</sup> AND JEREMY WITZENS<sup>1,\*</sup>

<sup>1</sup>*Institute of Integrated Photonics, RWTH Aachen University, Sommerfeldstr. 18/24, 52074 Aachen, Germany*

<sup>2</sup>*Now at the School of Electronic Engineering, Bangor University, LL57 1UT, UK*

<sup>3</sup>*Institute of Semiconductor Electronics, RWTH Aachen University, Sommerfeldstr. 18/24, 52074 Aachen, Germany*

<sup>4</sup>*Institute of Physics (IA), RWTH Aachen University, Sommerfeldstr. 16, 52074 Aachen, Germany*

\*[jwitzens@iph.rwth-aachen.de](mailto:jwitzens@iph.rwth-aachen.de)

**Abstract:** We report on the monolithic integration of a new class of reflowed silica microtoroid resonators with silicon nanowaveguides fabricated on top of the silica film. Connectivity with other silicon photonics devices is enabled by inversion of the toroid geometry, defined by etching a circular opening rather than a disk in an undercut silica membrane. Intrinsic quality factors of up to 2 million are achieved and several avenues of process improvement are identified that can help attain the higher quality factors ( $> 10^8$ ) that are possible in reflowed microtoroids. Moreover, due to the microtoroid being formed by standard microfabrication and post-processing by local laser induced heating, these devices are in principle compatible with monolithic co-fabrication with other electro-optic components.

© 2018 Optical Society of America under the terms of the [OSA Open Access Publishing Agreement](#)

## 1. Introduction

High Quality (Q-)factor resonators have a wide range of applications in communications and sensing. Nonlinear wavelength conversion by means of Four Wave Mixing (FWM) can, for example, lead to the formation of phase locked optical combs [1] that can be used as frequency references [2], multi-carrier sources for optical communications [3], or as multi-frequency sources for coherent spectroscopic sensing [4,5]. Other applications consist e.g. in resonant micro-optic gyroscopes [6], label free biomolecular sensing [7,8], narrow linewidth lasers with external resonant feedback [9,10], tunable delay lines used in signal buffering [11], optical or Radio-Frequency (RF) phase arrays [12], or other microwave photonics applications [13].

For all of these applications, obtaining a high Q-factor is critical, as it reduces the threshold for parametric comb generation, increases the obtainable time delays, increases the sensitivity of refractive index sensing and improves the frequency discrimination that can be obtained from the resonator. The size of the resonator also matters, with smaller devices being often preferred as it reduces the threshold for parametric generation (scaling as  $Q^2/V$  with  $Q$  the Q-factor and  $V$  the mode volume) and increases the Free Spectral Range (FSR). To date, the highest Q-factors, on the order of  $10^9$ , have been obtained with discrete resonators formed by macroscopically polishing crystalline materials such as  $\text{CaF}_2$  or  $\text{MgF}_2$  [14]. The highest Q-factors for smaller, chip-scale devices, in excess of 100 million, have been achieved with microtoroids obtained by melting and reflowing an  $\text{SiO}_2$  membrane with a  $\text{CO}_2$  laser [15]. Since these microtoroids are formed by minimization of the surface tension energy

of the molten  $\text{SiO}_2$ , they feature very little roughness, minimizing scattering induced optical losses. As a drawback, these resonators typically need to be coupled to a free standing tapered fiber, resulting in complex component assembly and preventing monolithic chip-scale integration with further photonic devices within a Photonic Integrated Circuit (PIC). Prior attempts have been made to couple these microtoroid resonators with on-chip waveguides, so far with mixed success: Microtoroids have been coupled to on-chip silica waveguides formed by the same reflow process as the microtoroids themselves [16] with demonstrated Q-factors of  $\sim 4$  millions. While this does facilitate packaging of the device – since it can now be edge coupled rather than requiring suspension of the tapered fiber right next to the resonator – arbitrary waveguide routing for forming complex on-chip devices remains difficult and electro-optic functionality (e.g. high-speed modulation) in this configuration does not seem possible. Microtoroid shaped resonators have also been made based on thermal annealing of silicon microdisks, but waveguide coupled devices only featured Q-factors up to 110,000 [17]. While Q-factors up to  $3 \times 10^6$  have since also been shown with Si based resonators [18], Si based devices suffer from Two-Photon Absorption (TPA) at high optical power levels, making them unsuitable for cascaded FWM, i.e., comb formation.

For these reasons, another PIC platform based on silica clad waveguides with a Silicon Nitride (SiN) core has more recently received prominent attention for parametric comb generation. On-chip comb generation with SiN waveguides [19] as well as with high index glass waveguides [20] was first shown in 2010 with high-confinement waveguides engineered to feature the required anomalous dispersion for comb formation. Q-factors in high confinement SiN platforms have since been improved to several millions by means of various process improvements, the photonic damascene process standing out as a particularly elegant method [21]. For applications in which high confinement, anomalous dispersion, or large FSR are not needed, low confinement SiN waveguides with Q-factors of up to 80 million can also be used [22]. More recently, Q-factors of up to 67 million have also been achieved in high confinement SiN waveguides, resulting in parametric oscillation thresholds below a mW [23]. Furthermore, SiN waveguides can be combined with electro-optically enabled Silicon Photonics (SiP) technology by defining silicon and SiN waveguides in a vertically coupled multi-layer stack [24], however the ultra-high Q-factors achieved in standalone SiN platforms have not yet been obtained in this combination. Waveguide coupled resonators with a record Q-factor of 200 million have been very recently shown in the form of silica wedge resonators coupled to a SiN waveguide [25], however a path to integration with silicon based electro-optically active PICs has not yet been shown. Thus, the combination of ultra-high Q-resonators suitable for low threshold parametric comb generation (requiring in particular suppressed TPA) with electro-optic devices in a monolithically integrated SiP chip remains an outstanding challenge. While elegant solutions have been found for combining functionalities in multi-chip assemblies, e.g. by means of photonic wire bonds [3], to the best of the authors' knowledge solutions have not yet been found to monolithically combine low threshold parametric comb generation, compatible with the pump power levels generated from a semiconductor laser diode, with a fully functional SiP platform on a single chip. With this objective in mind, we investigate the integration of reflowed silica microtoroids, in principle compatible with extremely high-Q factors and low threshold comb generation, in standard silicon nanowire waveguide based SiP technology.

## 2. Inverted microtoroid concept and high-level design choices

In this paper, a novel type of silica based microtoroid resonator is reported which can be monolithically coupled to a waveguide and is compatible with integration in a fully functional SiP platform. The notable feature of this architecture is that the conventional microtoroid geometry is inverted, such that the resonator is formed by thermal reflow at the circumference of an opening etched in a suspended silica membrane rather than at the circumference of a disk. The resulting device is coupled monolithically to a previously fabricated on-chip silicon

waveguide that can be routed to and from the resonator without topological constraints, as enabled by the latter's inverted geometry (Figs. 1 and 2).

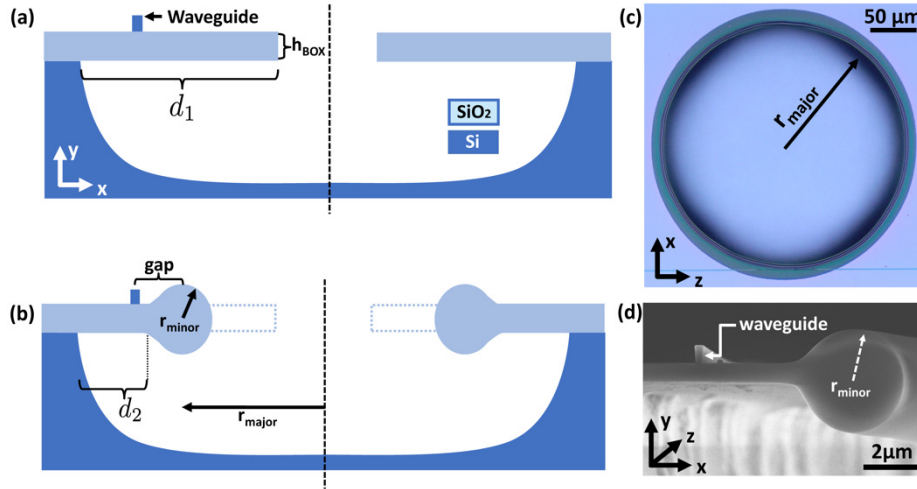


Fig. 1. Overview of the inverted microtoroid reflow process. Schematic cross-section of undercut SOI-BOX layer and waveguide prior to (a) and after (b) thermal reflow with a CO<sub>2</sub> laser. (c) Microscope top-view image of a melted microtoroid. (d) SEM cross-section image of a cleaved microtoroid.

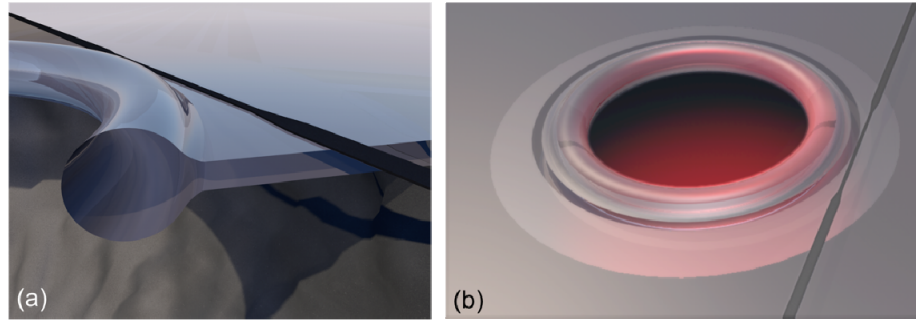


Fig. 2. 3D rendering of the proposed waveguide coupled inverted microtoroid with (a) a cross-section through the device and (b) a top view. These renderings also show the geometry of the waveguide in the coupling region, which is tapered down upstream of the microtoroid after entering the undercut region and tapered back up downstream of the microtoroid before exiting the undercut region.

Figure 1 also introduces geometrical parameters that define the shape of the resonator: The major radius  $r_{major}$ , the minor radius  $r_{minor}$ , the initial undercut depth  $d_1$  and the remaining undercut after reflow  $d_2$ , as well as the Buried Oxide (BOX) thickness  $h_{BOX}$ . Assuming the SiO<sub>2</sub> to conserve its volume during reflow, we can simply estimate  $r_{minor}$  as

$$r_{minor} = \sqrt{(d_1 - d_2) h_{BOX} / \pi} \quad (1)$$

thus relating the geometry of the microtoroid to the amount of reflowed silica.

The primary figure of merit of the device is its Q-factor, which, here, is highly dependent on the internal bending losses of the resonator. Indeed, a primary difference between the inverted geometry shown here compared to conventional microtoroids is a much weaker confinement and thus a higher propensity towards optical bending losses [Fig. 3]. In a conventional microtoroid, the mode is pressed towards the outer rim of the core located opposite to the suspended silica membrane. This region features a high dielectric index

contrast between the silica and the surrounding air. On the contrary, in the case of an inverted microtoroid, the mode is pressed towards the silica membrane, whose optical modes have effective indices much closer to the microtoroid's, resulting in increased leakage into the membrane modes.

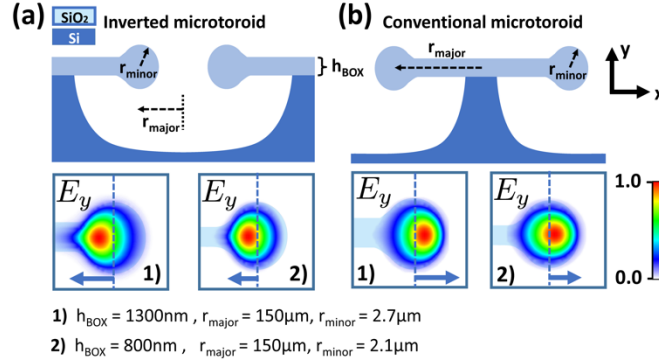


Fig. 3. Comparison of  $TM_0$  ground-modes between (a) an inverted microtoroid and (b) a conventional microtoroid (from optical FEM mode-solves in cylindrical coordinates). The mode confinement towards the outer region of the inverted microtoroid's circumference is weaker since the mode is pressed towards the suspended silica membrane. This effect becomes even more pronounced for thicker BOX layers, compare case 1) with 2).

In order for the bending losses not to become the limiting factor for the microtoroid's Q-factor without requiring excessively large bending radii, the BOX thickness should be thin enough, since reduction of its thickness reduces both the effective index of the membrane slab modes and their spatial overlap with the microtoroid mode, thus minimizing optical leakage into the slab. On the other hand, reduction of the BOX thickness also increases substrate leakage losses of Si waveguides fabricated elsewhere on the chip [26]. Therefore, a tradeoff exists between reducing the bending losses of the microtoroid resonator and reducing Si waveguide substrate leakage losses. Figure 4(a) shows the simulated bend loss limited loaded quality factor  $Q_{Bend}$ , assuming critical coupling to the bus waveguide, as a function of the BOX thickness for two major radii  $r_{major}$  of 125  $\mu m$  and 150  $\mu m$  and for both the Transverse Electric (TE) and the Transverse Magnetic (TM) ground modes  $TE_0$  and  $TM_0$ .

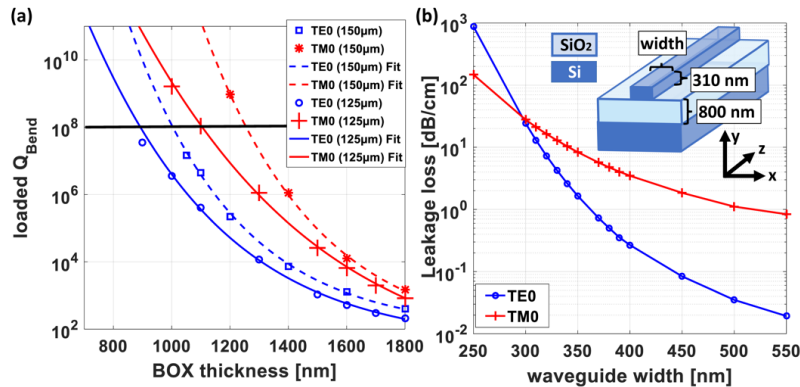


Fig. 4. (a) Simulated bending loss limited loaded quality factor for an inverted microtoroid for the  $TE_0$  (blue) and  $TM_0$  (red) modes as a function of the BOX thickness  $h_{BOX}$ . The core radius  $r_{minor}$  is implicitly varied according to Eq. (1). The parameter  $d_1$  is assumed to be 22  $\mu m$  and  $d_2$  is assumed to be 5  $\mu m$ . The solid lines correspond to a major radius of  $r_{major} = 125 \mu m$  and the dashed lines to a major radius of  $r_{major} = 150 \mu m$ . (b) Simulated optical leakage losses of the  $TE_0$  and  $TM_0$  ground modes of a 310 nm thick Si interconnect waveguide as a function of its width assuming an 800 nm BOX thickness. A 3D schematic of the unclad simulated waveguide is shown in the inset.



A  $Q_{Bend}$  of more than a 100 million is ideally targeted, since this is on the order of the highest Q-factors measured on conventional microtoroids and can be considered as the limit constrained by material properties such as impurities, residual roughness, SiO<sub>2</sub> redeposition or water adsorption. From Fig. 4 it can be concluded that the BOX thickness should be smaller than 0.9  $\mu\text{m}$  (1.0  $\mu\text{m}$  for  $r_{major} = 150 \mu\text{m}$ ) for the transverse electric (TE<sub>0</sub>) ground mode and smaller than 1.1  $\mu\text{m}$  (1.3  $\mu\text{m}$  for  $r_{major} = 150 \mu\text{m}$ ) for the transverse magnetic (TM<sub>0</sub>) ground mode. The core radius  $r_{minor}$  is implicitly varied according to Eq. (1). The parameter  $d_1$  is assumed to be 22  $\mu\text{m}$  and  $d_2$  is assumed to be 5  $\mu\text{m}$  (typical values as seen in the following), resulting e.g. in  $r_{minor} = 2.1 \mu\text{m}$  for an 800 nm BOX thickness. The actual layer thicknesses of our Silicon-on-Insulator (SOI) chips were also constrained by our vendor's offerings, so that we decided on using a 310 nm Si device layer thickness and an 800 nm BOX layer thickness.

Since 800 nm is substantially thinner compared to the 2  $\mu\text{m}$  BOX of SOI wafers more commonly used in SiP, particular attention has to be given to potential substrate coupling losses of Si interconnect waveguides fabricated in the device layer of the chip. Figure 4(b) shows the simulated losses for the TE<sub>0</sub> and TM<sub>0</sub> modes as a function of the waveguide width. The inset is a schematic representation of the simulated unclad Si interconnect waveguide. While the substrate coupling losses are significantly higher for the TM polarization, they drop below 1 dB/cm for a waveguide width of 500 nm and above, even for the TM<sub>0</sub> mode. As the focus of this work is primarily on TM polarized light due to the reduced microtoroid bending losses, interconnect waveguide widths above 500 nm were chosen for most of the waveguide regions (other than the edge coupling and waveguide-to-toroid coupling sections).

Prior to moving on to the experimental and more detailed modeling sections, it should be pointed out that high-Q resonances do not necessarily always correspond to the TM<sub>0</sub> (also denoted as TM<sub>00</sub>) ground mode: While increasing the number of lobes in the horizontal direction results in a reduced effective index and higher bending losses, the TM<sub>01</sub> mode with two lobes in the vertical direction, while having a reduced effective index, also maintains low bending losses due to its modified symmetry preventing it from coupling into the ground mode of the undercut SiO<sub>2</sub> slab, provided the symmetry of the microtoroid relative to the horizontal center plane is not broken. Since the lowest odd slab mode has a higher effective index and is less confined, this reduces bending losses. In practice the microtoroid can end up being off-center relative to the slab's center plane, in which case TM<sub>01</sub> Q-factors can be significantly reduced. The TM<sub>01</sub> mode also has a reduced coupling to the interconnect waveguide, even though, due to the waveguide being off-center and breaking the vertical symmetry, it remains non-zero. Typical TM<sub>10</sub> and TM<sub>01</sub> modes are illustrated in Fig. 5.

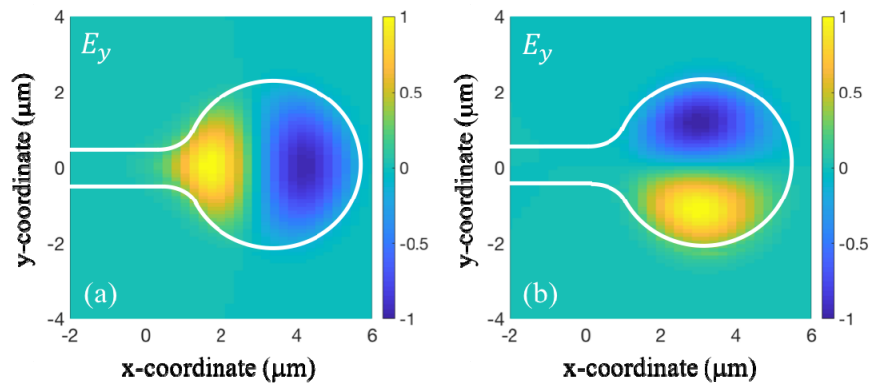


Fig. 5. Higher order inverted microtoroid modes. (a) shows the TM<sub>10</sub> mode with two horizontal lobes and (b) shows the TM<sub>01</sub> mode with two vertical lobes. While the TM<sub>01</sub> mode also has a lower effective index than the TM<sub>00</sub> mode, its symmetry reduces coupling to the slab, so that it typically has comparable high Q-factors to the latter. Here,  $\lambda_0 = 1.55 \mu\text{m}$ ,  $r_{minor} = 2.3 \mu\text{m}$ ,  $r_{major} = 145 \mu\text{m}$ ,  $h_{BOX} = 800 \text{ nm}$ .

### 3. Fabrication process

Fabrication starts with a high-grade, industry compatible 8 inch SOI wafer with a nominal silicon device layer thickness of 310 nm and a 10 nm  $3\sigma$  deviation. The BOX layer is specified as having a target thickness of 800 nm with a 6 nm  $3\sigma$  deviation.

The first part of the fabrication flow can be subdivided into four process modules carried out entirely in a cleanroom environment: The waveguide definition, the circular opening definition, the silicon undercut, and the final dicing and cleaning step [Fig. 6]. The second part of the fabrication consists in the CO<sub>2</sub> laser reflow carried out in a dedicated setup. Since laser induced heating is confined to the immediate vicinity of the microtoroid, it is in principle compatible with more complex PICs containing additional electro-optic or heterogeneously integrated active devices.

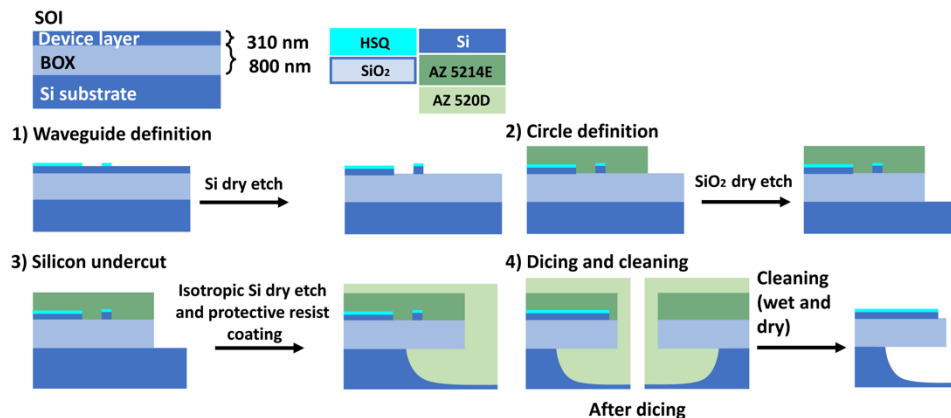


Fig. 6. Summary of fabrication flow: 1) The chip is coated with Hydrogen Silsesquioxane (HSQ) resist and is patterned with EBL. Subsequently the pattern is transferred into the underlying silicon layer by dry etching. 2) The chip is spin-coated with AZ 5124E resist, and optical lithography is used to define circular openings (for microtoroid formation) and linear trenches (for dicing lanes). Subsequently, the pattern is transferred into the BOX by dry-etching. 3) The previously defined trenches and circles are undercut by isotropic dry-etching of the underlying silicon substrate. For further processing, the chip is protected with AZ 520D resist. 4) Finally, the chip is diced along its predefined dicing lanes and cleaned.

After singulating the wafer into 20 by 20 mm chips, the process proceeded as follows:

- (1) Etching of Si waveguides, based on a previously defined Electron Beam Lithography (EBL)-pattern, with a mixed gas process using SF<sub>6</sub> and C<sub>4</sub>F<sub>8</sub> and a processing temperature close to room temperature.
- (2) Etching of circular openings through the BOX using Reactive Ion Etching (RIE) in a CHF<sub>3</sub> plasma. Ion milling caused by the addition of inert argon improves the anisotropy of the etch [27].
- (3) Undercut of the Si below the BOX layer by about 30  $\mu$ m in the lateral direction with SF<sub>6</sub> in an Inductively Coupled Plasma (ICP) RIE, with zero acceleration voltage resulting in an isotropic chemical etch. There is no oxygen involved in the etch process, as it would attack the photolithography resist used to protect the silicon structures. The manufacturer of the ICP tool Oxford Instruments specifies the selectivity between Si and SiO<sub>2</sub> of a comparable process using a PlasmaPro 100 Cobra ICPRIE system to be larger than 500:1.
- (4) Finally, the chips are diced to allow access to the edge coupling tapers and subsequently cleaned.

Importantly, the BOX layer dry etch and the Si undercut are also applied to the dicing lanes, so that edge couplers used to couple in and out of the waveguides are also undercut. Nonetheless, edge couplers were able to systematically withstand dicing and cleaning without breakage, after design improvements were introduced to increase their mechanical stability (see next section).

For all the etching processes, an Oxford PlasmaPro 100 ICP system with an ICP source diameter of 300 mm was used. A silicon wafer was used as carrier for the chips, potentially allowing scaling up of the process from chip to wafer level without changing process biases, as the underlying silicon carrier wafer was etched simultaneously resulting in the same loading effects during critical silicon etches. In fact, up to four chips were processed in parallel without noticeable process bias. Fomblin oil was used for establishing thermal coupling between the chips and the carrier wafer, cooling them down to 15-20 °C. Table 1 summarizes the process parameters:

**Table 1. Etch process parameter**

Etch Step	ICP Power	RIE Power	DC Bias	Gas Flow	Chamber Pressure
Si Waveguides	1200 W	30 W	240 V	SF <sub>6</sub> : 25 sccm C <sub>4</sub> F <sub>8</sub> : 50 sccm	20 mTorr
SiO <sub>2</sub>	0 W	100 W	430 V	CHF <sub>3</sub> : 50 sccm Ar: 50 sccm	30 mTorr
Si undercut	2000 W	0 W	-	SF <sub>6</sub> : 50 sccm	30 mTorr

A subsequent CO<sub>2</sub>-laser reflow process shapes the microtoroids by surface tension, removing residual roughness to a very large extent. The previously undercut silica membrane [Fig. 1(a)] is surface-normal-irradiated with a nearly Gaussian shaped focused beam ( $\lambda = 10.6 \mu\text{m}$ ). Typical beam radii used in this work are in the range of 150  $\mu\text{m}$  to 400  $\mu\text{m}$ , depending on the position of the focusing optics, with total optical power in the range of 10 W to 20 W leading to power density levels of about 100-400 W/mm<sup>2</sup> at the undercut membrane.

Selective absorption of the laser light by the SiO<sub>2</sub> combined with an increased thermal resistivity to the substrate from the rim of the undercut membrane leads to local melting at its periphery. The surface tension during reflow then yields the microtoroidal shape. The optical absorption of fused silica is about 100 times stronger than that of silicon at a wavelength of 10.6  $\mu\text{m}$  [28,29]. Even thin silica membranes can absorb light at this wavelength very efficiently [29]. This way, the supporting silicon is acting as a heat sink for the silica membrane and the silicon is not melted or otherwise physically affected due to its low optical absorption and high thermal conductivity. As the thermal transmittance of fused silica is significantly reduced with increasing temperature [29], the melting process starts suddenly due to thermal runaway when a critical laser power level is reached [30] and the silica is heated up above its melting temperature of about 1650 °C [31].

#### **4. Improved fabrication with thermal flow control and mechanical stabilization by means of a silicon frame**

A supporting structure is introduced in the Si device layer with the dual function of acting as a heat spreader for fine-tuning of the silica membrane melting process as well as to provide mechanical stabilization of the freestanding membrane. One of the challenges of waveguide-coupled microtoroid fabrication is to obtain a prescribed gap between the toroid and the coupled Si waveguide. Since the reflow-process is self-limiting with dynamics determined by heat sinking through the Si substrate, local modification of the thermal conductivity increases the level of control over the final geometry. Moreover, the region where the silica membrane merges with the non-undercut Si substrate is subjected to high local strain, which, in addition to deformation of the membrane (wobbling, see Fig. 7), can even lead to breakage in extreme cases. An annular shaped Si frame surrounding the microtoroid and the Si waveguide is



etched into the Si device layer at the same time as the waveguide and carries out both functions (see Figs. 8(b) and 10(b) for micrographs before and after reflow).

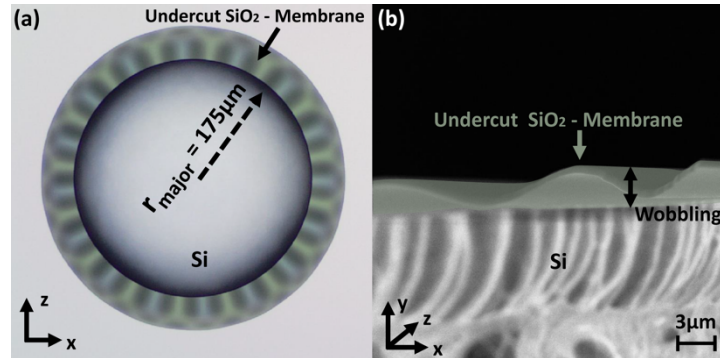


Fig. 7. Wobbling of the undercut silica membrane in the absence of a stabilizing frame. (a) Top view taken with an optical microscope and (b) side view SEM image revealing wobbling with an amplitude of several  $\mu\text{m}$ .

We first describe the mechanical problem: Wobbling of the membrane after undercut due to residual built-in strain in the thermally grown BOX was observed in earlier fabrication runs as shown in Fig. 7. Even though this wobbling typically was strongly suppressed after reflow, it led to concerns that residual wobbling might lead to a reduction of the resonator Q-factor. In addition to the wobbling, broken membranes were observed in extreme cases [Fig. 8(a)] with cracks first forming at the rim of the undercut region where the silica film merged with the substrate, with potentially very high strains occurring in that region. As the severity of the wobbles increases with the depth of the undercut, this can restrict the addressable design space. For these reasons, it was concluded that it would be highly advantageous to have a mechanically stabilizing structure in the form of a frame etched into the Si device layer and straddling both the undercut and non-undercut regions of the silica film [Figs. 8(b) and 8(c)]. From these figures it is apparent that the wobbling and the cracking of the freestanding silica membrane is suppressed. This effect was consistently observed and greatly increased the reliability of the fabrication process.

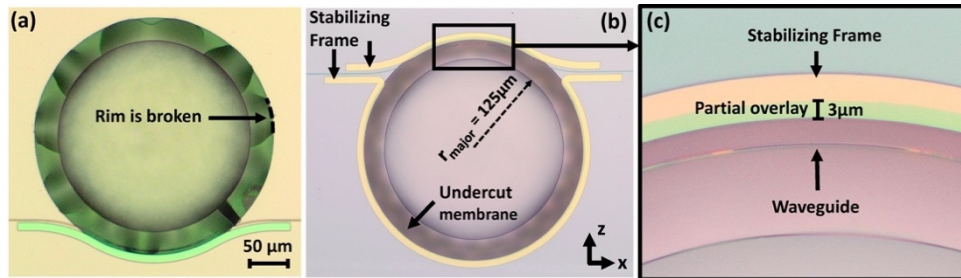


Fig. 8. Mechanical stabilization of the undercut membrane by means of a Si frame. (a) Extreme case of a membrane without a stabilizing frame cracking prior to reflow. (b) Intact membrane with much reduced wobbling by means of a stabilizing frame. (c) Detailed view showing the Si frame reaching  $3\ \mu\text{m}$  into the undercut region of the silica film (blue: non-undercut region with no Si frame, yellow: non-undercut region with Si frame, green: undercut region with Si frame, light mauve: undercut region without Si frame, deep mauve: etched away silica film).

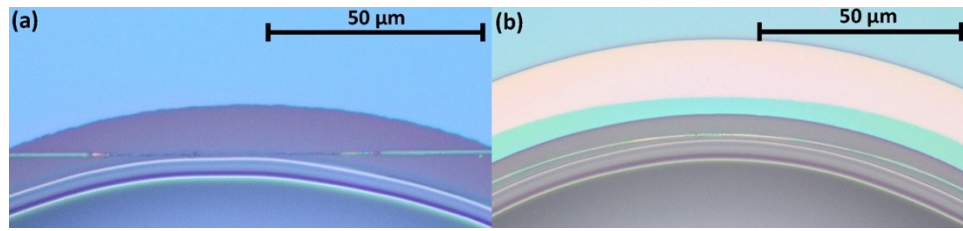


Fig. 9. Reflow results for waveguide coupled inverted silica microtoroids with (a) a straight coupler and (b) a weakly tapered gap coupler. In case of a straight coupler (a), the coupling section itself acts as a disturbance to the melting process and locally deforms the microtoroid. A weakly tapered gap coupler (b) on the other hand fits well to the natural shape of the microtoroid and results in a weakly tapered (adiabatic) deformation.

Several difficulties are associated with the uniformity of the thermal reflow process: During this process, the silica membrane melts until the microtoroid moves sufficiently close to the rim of the undercut region, at which point improved heat sinking slows down and eventually almost stops the reflow process. This also means that any non-uniformity in the thermal heatsinking environment is transferred to the shape of the microtoroid.

One such disturbance that is systematically present by design in case of a straight Si waveguide junction is the Si waveguide itself, which locally increases heat sinking [Fig. 9(a)]. Adiabatically tapering the distance between the microtoroid and a curved waveguide effectively improves this [Fig. 9(b)]. Moreover, this adiabatic tapering also reduces the excitation of higher order modes inside the microtoroid and thus the excess losses of the junction, which can have a strong effect on the Q-factor of ultra-high-Q resonators [22]. Further difficulties reside in the definition of the undercut: For one, large roughness arising on the Si edge in the undercut step gets transferred to the microtoroid shape. While significant progress was made in the etch smoothness after process optimization, some residual roughness remains. More importantly, the circular openings etched into the silica film were defined by optical lithography and featured a misalignment of up to 1  $\mu\text{m}$  relative to the waveguide layer, offsetting the position of the reflowed microtoroid relative to the Si bus waveguide. Lastly, it proved difficult to control the extent of the undercut with sub- $\mu\text{m}$  accuracy. Given all these stacked process variations, it appeared highly desirable to define the microtoroid shape relative to a fiducial etched at the same time as the waveguide. This role is also fulfilled by the previously introduced stabilizing Si frame, as it reduces the thermal resistance to the substrate once the microtoroid approaches its vicinity and stops the reflow process. Since it is defined at the same time as the waveguide, it greatly improves the overlay accuracy between waveguide and reflowed microtoroid. Moreover, since the anisotropic dry etch used for waveguide definition has nanometric roughness, transfer of roughness to the microtoroid via the melting process is also improved.

For validating the heat spreading functionality of the Si frame, a 3D thermal simulation was done corresponding to the modeling in cylindrical coordinates of the device cross-section shown in the inset of Fig. 10(a) with a Finite-Element Method (FEM) using the commercially available COMSOL package. In the simulation setup, the microtoroid core is heated by a constant heat source calibrated to lead to a maximal temperature of approximately 1650  $^{\circ}\text{C}$  at the microtoroid's surface when the Si frame is not present and the distance  $d_2$  between the edge of the microtoroid and the edge of the undercut (see Fig. 1) is 8  $\mu\text{m}$ . The simulation is done for different microtoroid to Si-frame distances  $d_3$  in order to monitor the effectiveness of the Si-frame as a heat spreader (see Fig. 10) for a constant, typical Si-frame width of 10  $\mu\text{m}$ . The Si-frame overlays with the undercut region by an amount labeled as *Offset* in Fig. 10, i.e., when *Offset* equals 0 the Si-frame is located entirely in the non-undercut region and when *Offset* equals 10  $\mu\text{m}$  the Si-frame is located entirely in the undercut region. As *Offset* is varied from 2  $\mu\text{m}$  to 8  $\mu\text{m}$  (emulating varying lithographic overlay and undercut process variations), the distance  $d_3$  that results in the 1650  $^{\circ}\text{C}$  toroid temperature required to sustain melting of the

silica varies by less than 1  $\mu\text{m}$ , with an average value around  $\sim 10.7 \mu\text{m}$ . In other words, the sensitivity of the toroid-to-waveguide distance on the overlay accuracy between the e-beam lithography defining the waveguide and the optical lithography defining the circular silica film opening, as well as on the depth of the undercut, is reduced by more than a factor 6, greatly increasing the repeatability of the achieved waveguide-to-toroid coupling strengths.

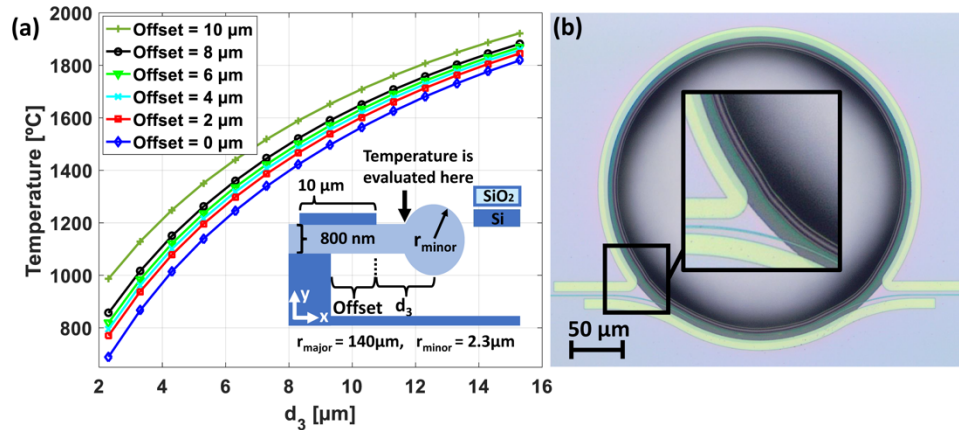


Fig. 10. (a) Simulation of the effect of the Si-frame on heat sinking during microtoroid reflow. The cross-section shown in the inset is simulated in cylindrical coordinates. In the simulation setup, the microtoroid itself is designed as a heat source calibrated to result in the typical temperatures for high-purity silica reflow ( $\sim 1650^\circ\text{C}$ ). The distance  $d_3$  between the Si-frame and the toroid is varied and the simulation repeated for different values of the parameter *Offset* that would in practice result from fabrication tolerances (overlay between lithography steps and depth of undercut). It is apparent that even though a large span of *Offset* is considered, the curves remain quite clustered, pointing to the distance to the Si-frame as the main determining factor. (b) Microscope image of a fully fabricated device, with the inset showing in particular a small residual deformation in the toroid shape where the waveguide is routed away and the Si-frame thus interrupted.

After implementation of the Si-frames, we observed that homogeneous melting of the microtoroids was more consistently achieved and that the control over the microtoroid-to-waveguide distance was improved. One difficulty remains however with handling the two corner regions in which the waveguide is routed away from the microtoroid (see inset in Fig. 10(b)). Since the Si-frame has to be interrupted in that region, it can actually locally make things worse by introducing a sharp discontinuity in the thermal environment, resulting in a deformation of the microtoroid shape at that point (a notch with a locally decreased bending radius at its tip). In order to alleviate this, we extended the heat spreader along both sides of the departing waveguide, thereby locally increasing its effectiveness to partially compensate for the reduced heat sinking in the middle of the gap. This approach relies on sufficient averaging in the thermal environment to smooth out these micron-scale variations. It did however prove necessary to carefully dial-in the reflow parameters (beam diameter and power) to obtain good, notch free reflow.

## 5. Detailed device design and experimental characterization

### 5.1 Edge couplers and interconnect waveguides

Inverse tapered edge couplers were designed and fabricated in the same fabrication process in order to couple light onto the chips. In order to avoid the need of polishing after singulation of the chips, which would have been problematic due to the presence of relatively fragile undercut silica membranes, the dicing lanes were also predefined by means of the silica etch and the silicon undercut (respectively steps 2 and 3 in the process flow described in section 3). This results in the inverse tapers also being located on an undercut, relatively thin 800 nm

thick SiO<sub>2</sub> membrane. This and the absence of cladding result in an asymmetric field distribution inside the taper and a slight degradation of the coupling efficiency [32,33].

Figure 11(a) shows a top view of an edge-coupler. The waveguide is tapered down from 570 nm inside the chip to about 90 nm at the tip of the coupler [Fig. 11(b)]. A 3D schematic representation and a schematic cross-section of the edge-coupler can be found in Figs. 11(c) and 11(d). The inverse taper is situated mainly on top of the freestanding silica membrane undercut by a length  $d_1$  identical to the one labeled in Fig. 1. In order to protect the membrane from breaking, silicon stabilizers are defined in the silicon device layer on either side of the waveguide, similarly to the stabilizing Si frame applied to the microtoroids. Minimizing the distance  $s$  from the tip of the edge-coupler to the outer rim of the membrane is crucial for maintaining a high coupling efficiency. The distance  $s$  is usually on the order of 2–3  $\mu\text{m}$ , wherein a minimum is required for process related reasons to protect the Si waveguide from the Si undercut step, i.e., its tip needs to be fully covered by the protective photoresist.

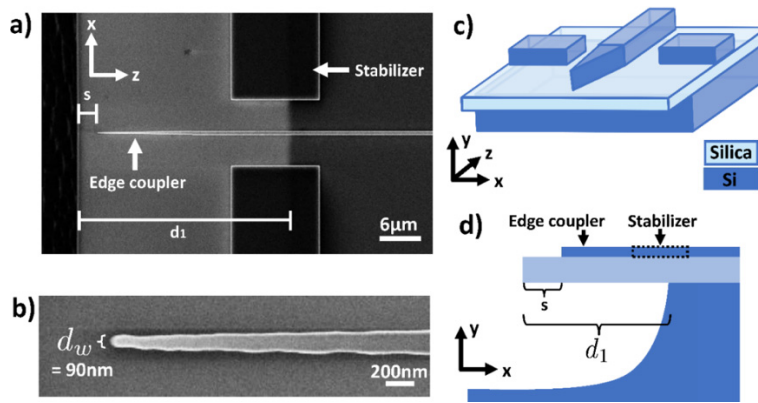


Fig. 11. Inversely tapered edge-coupler. (a) Top view SEM image of the edge-coupler. The edge-coupler tip is positioned on top of a freestanding silica membrane and recessed by a distance  $s$  from its edge. For avoiding cracking of the membrane, dedicated stabilizers are defined in the silicon device layer. (b) Zoomed image on the edge-coupler's tip narrowing down to a width of about 90 nm. (c) 3D-schematic of the edge-coupler. (d) Schematic of a cross-section of the edge-coupler taken along its longitudinal direction.

The target for the tip width  $d_w$  was set to be 90 nm since it resulted in an acceptable coupler performance, could be reproducibly fabricated with EBL, and the aspect ratio of the tip width to height is high enough to result in adequate mechanical stability. The transformed optical waveguide mode at the edge of the chip has a  $(1/e^2)$  Mode Field Diameter (MFD) of 4.87  $\mu\text{m}$  in the x-direction and 2.07  $\mu\text{m}$  in the y-direction. The optical insertion loss to a lensed fiber (2.5  $\mu\text{m}$  MFD and 14  $\mu\text{m}$  working distance) is evaluated to be on the order of 1.8 dB based on simulations (including penalties due to the non-Gaussian nature of the transformed waveguide mode).

The fiber-to-fiber optical losses induced by 6 mm long on-chip reference waveguides (with a 500 nm width) and 2 edge couplers were consistently below 15 dB, so that we estimate waveguide losses to be on the order of 15 dB/cm. It should be noted here that optimization of the EBL and etching processes for minimization of the silicon waveguide roughness was not an objective here, as it does not impact the performance of the developed microtoroids.

## 5.2 Microtoroid coupler design

General design considerations for the microtoroids themselves have already been described in section 2, however designs for the microtoroid to Si waveguide junction have not yet been described. Design of these junctions is critical, as not only does the coupling strength need to be dialed in according to the microtoroid's internal losses in order to obtain sufficiently deep



resonances in the device's transfer function (ideally critical coupling), but excess losses caused by the microtoroid-to-waveguide junction should also be minimized. These are expected to be more of a concern here compared to tapered fiber coupled microtoroids due to the high refractive index of the Si waveguide core resulting in increased levels of scattering from the microtoroid core in an abrupt junction.

The excess losses per pass of the directional coupler are denoted as  $\gamma$  in the following. These losses can occur due to scattering losses or coupling into unwanted higher order microtoroid modes and are limiting the maximum attainable loaded quality factor  $Q_L$  [22]. In the case where the excess losses  $\gamma$  are on the same order as the total resonator round trip loss  $\alpha L$  (where  $\alpha$  is the linear loss coefficient and  $L$  is the length of the resonator), the loaded quality factor  $Q_L$  is substantially worsened. Especially for high-Q-factor resonators, this can become an issue. The coupler design itself can be optimized in view of minimizing these excess losses. In this work, two different coupler designs are considered, the straight coupler and the weakly tapered gap coupler that has been previously shown to result in lower excess losses [22]. In the latter, the mode phase velocity mismatch (difference in the propagation-constants  $\beta$ ) between the two arms of the coupler is reduced over a longer coupling length, which leads to a more efficient coupling into the fundamental mode and suppresses excitation of higher order modes. Also, the weak tapering of the gap yields a more progressive transition region from the input waveguide to the coupling section, which potentially further lowers the excess losses compared to other coupler designs.

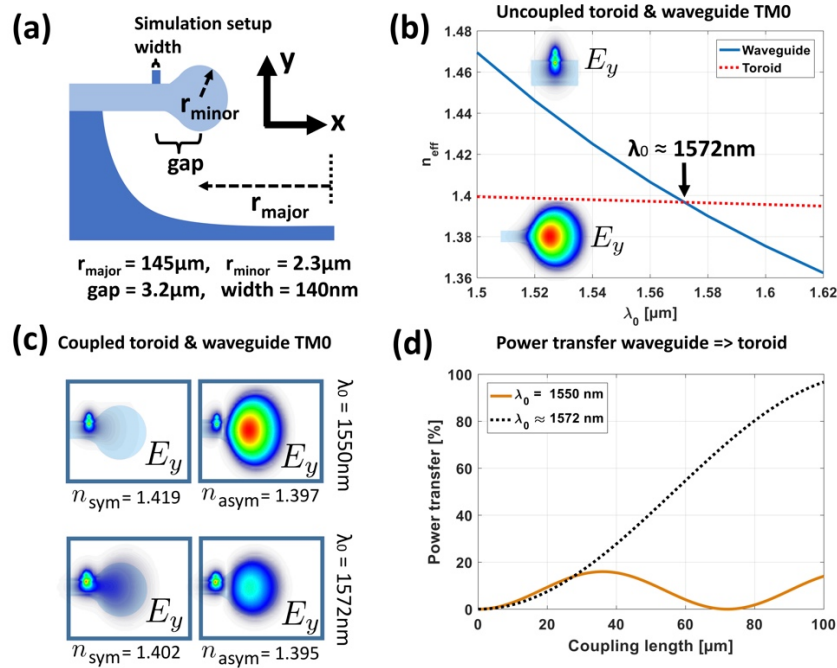


Fig. 12. Simulated optical power transfer between the Si bus waveguide and the inverted microtoroid as a function of the coupling length and wavelength based on super-mode modeling with help of FEM in cylindrical coordinates. (a) Schematic of the simulation setup. (b) Effective index of the uncoupled Si waveguide (solid blue) and microtoroid (dashed red)  $\text{TM}_0$  ground modes. The effective indices are crossing at a wavelength of  $\lambda \approx 1572 \text{ nm}$ . (c) Coupled symmetric and antisymmetric  $\text{TM}_0$  super-modes for two different wavelengths of  $\lambda_0 = 1550 \text{ nm}$  and  $1572 \text{ nm}$ . (d) Maximum possible power transfer as a function of the coupling length between waveguide and microtoroid for the two selected wavelengths.

To maximize the optical power build-up inside the microtoroid, e.g. to minimize the threshold for parametric wavelength conversion, it is crucial to reach a coupling point at, or



close to critical coupling [34]. For conventional microtoroids, this can be achieved by adjusting the gap between a suspended tapered fiber and the resonator [34]. In an integrated solution, the gap is fixed and needs to be well targeted by design. For a proof-of-principle demonstration the coupling strength can be corrected to some extent by tuning the wavelength or the temperature. The silicon waveguide and silica microtoroid are made out of different materials. Since silicon has a substantially higher thermo-optic coefficient compared to silica, thermal tuning can be used for fine-tuning the coupling strength by moving in and out of the phase matching condition. Moreover, due to the high geometric dispersion of the tapered silicon waveguide, changing the wavelength can also serve to tune the coupling strength [35]. Designs described in the following are targeted to reach critical coupling at a wavelength of 1550 nm and room temperature, with further wavelength and temperature tuning applied experimentally to correct for deviations.

Figure 12(b) shows the simulated effective indices (FEM in cylindrical coordinates) of an uncoupled waveguide mode and an uncoupled microtoroid mode as a function of wavelength, obtained by either removing the Si waveguide from the simulation setup or by extending the silica film. The following geometric parameters are assumed:  $r_{major} = 145 \mu\text{m}$ ,  $r_{minor} = 2.3 \mu\text{m}$ ,  $gap = 3.2 \mu\text{m}$  (with gap as shown in Fig. 12(a) defined as the center-to-center distance, for experimental reasons as this quantity could be more precisely determined from micrographs). The width of the waveguide in the coupling section is 140 nm. The very strong geometric dispersion of the Si waveguide is visible. Phase matching is predicted to occur at 1572 nm. Figure 12(c) shows the field distributions for the symmetric and the antisymmetric super-modes of a Si waveguide coupled to a microtoroid at two selected wavelengths of  $\lambda_0 = 1550 \text{ nm}$  and 1572 nm. The theoretical maximum power transfer is about 16% at 1550 nm and reaches up to 100% at 1572 nm [Fig. 12(d)]. Therefore, even for a lithographically defined waveguide-to-toroid distance, phase matching can be achieved by tuning the wavelength if the gap is sufficiently close to target. Also, the desired coupling point can be accessed provided the coupling length is long enough (in this work it is on the order of  $60 \mu\text{m}$  for the weakly tapered junctions).

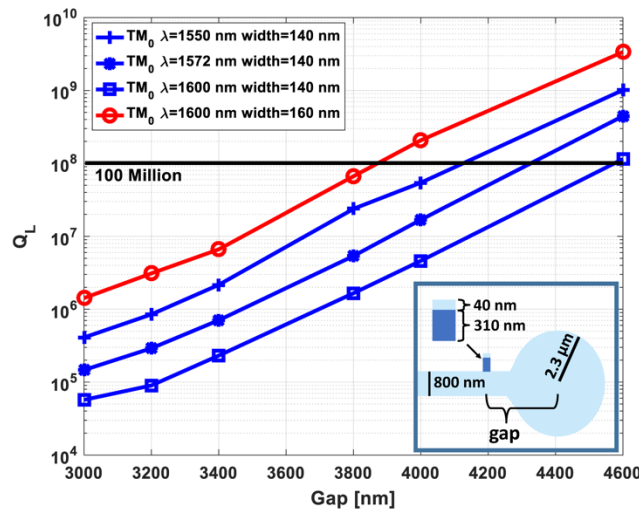


Fig. 13. Graph showing the waveguide-to-microtoroid gap required to obtain critical coupling as a function of the expected microtoroid quality factor.  $Q_L$  is the resulting loaded Q-factor, i.e., half the assumed intrinsic Q-factor assuming no excess coupling losses. Simulations were done with full 3D FDTD. The inset shows a schematic of the toroid and waveguide cross-section in the plane where the waveguide is closest to the toroid.

In order to take into account the full 3D geometry of the coupling section, 3D Finite Difference Time Domain (FDTD) simulations were performed assuming a weakly tapered Si

waveguide located at different gaps from the microtoroid. As before, the toroid has a major radius  $r_{major} = 145 \mu\text{m}$  and a minor radius  $r_{minor} = 2.3 \mu\text{m}$ . Inside the coupling section, the weakly tapered waveguide has a curvature 1.2 times larger than the major radius of the toroid. Figure 13 shows the gap (defined as the center-to-center distance) required to obtain critical coupling for a given loaded quality factor  $Q_L$  assuming no excess losses, as extracted from the simulated coupling strengths  $\kappa^2$  (i.e., assuming  $Q_L$  to be half the intrinsic Q-factor).

By comparing different tapered Si waveguide widths in the coupling section, it is apparent that for wider waveguides the light is more confined, therefore resulting in a lower coupling strength. By changing the wavelength within a range of 50 nm, the coupling strength can be adjusted for quality factors that differ by one order of magnitude, which is a very important feature since the intrinsic quality factor, as limited by fabrication related nonidealities, is difficult to predict a-priori. For example, a microtoroid separated by a fixed gap of 3400 nm from the center of a Si waveguide with a width of 140 nm can be critically coupled in case of real quality factors  $Q_L$  in the range  $2 \cdot 10^5$  to  $2 \cdot 10^6$  by changing the wavelength from  $\lambda_0 = 1550$  nm to  $\lambda_0 = 1600$  nm.

Since the coupling section is located on top of the undercut silica membrane [Fig. 14(a) inset], coupling to the Si wafer substrate is not an issue (since the Si-waveguide is tapered down in the coupling region, this could otherwise be a problem). However, since the waveguide width in the coupling section is chosen to verify phase matching with the microtoroid mode, and the waveguide's effective index is thus close to the refractive index of  $\text{SiO}_2$ , coupling of the waveguide mode into the underlying silica membrane can occur. Figure 14(a) shows the simulated effective index of a Si waveguide situated on top of a freestanding silica membrane as a function of its width. For a width above  $\approx 150$  nm the effective index rises above the refractive index of silica. While critical coupling is then no longer maintained, sufficient coupling strengths can still be obtained as shown in Fig. 13 for a 160 nm wide waveguide. In the fabricated devices, we taper the waveguide down to approximately 120-150 nm. At this point, the effective index of the silicon waveguide is already slightly below the bulk refractive index of silica, however the waveguide losses in the short coupling region remained small and did not present a problem for the experimental characterization (they are simulated as being below a few tens of a dB). Moreover, for a 120 nm wide waveguide, the  $1/e$  folding length of the  $E_y$  field is evaluated as being 450 nm in the x-direction, which gives an idea of the sensitivity of the coupling strength on the waveguide-toroid gap (about an order of magnitude every half micron as also seen in Fig. 13). Figure 14(b) shows an SEM image of a fabricated coupling section with a waveguide width of 120 nm.

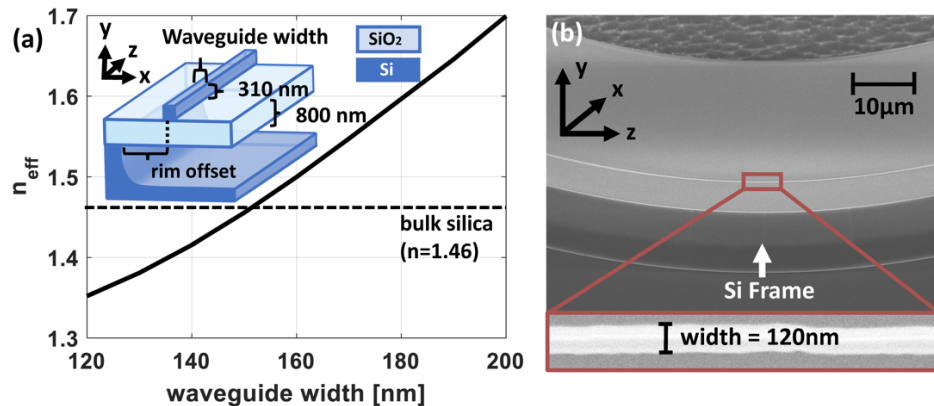


Fig. 14. (a) Effective index  $n_{eff}$  of the coupling section waveguide as a function of its width. The inset shows a 3D schematic of coupling section waveguide. (b) SEM image of fabricated coupling section (width = 120 nm) with attached Si Frame.

Another potential issue that needed to be validated by simulations was whether the stabilizing Si frame would spoil the resonator Q-factor due to the nearby presence of a high refractive index structure. We performed a series of simulations assessing the Q-factor of a microtoroid with a major radius of  $145\ \mu\text{m}$  and a minor radius of  $2.3\ \mu\text{m}$  as a function of the distance between the center of the toroid and the edge of the stabilizing frame,  $d_3$ . As seen in Fig. 15, the presence of the stabilizing frame is expected not to spoil even the highest expected Q-factors if  $d_3$  is larger than  $3\ \mu\text{m}$ , since the loaded Q-factor as limited by evanescent coupling to the stabilizing frame then stays above 100 million. Since in the fabricated devices reported here  $d_3$  was always larger than  $5\ \mu\text{m}$ , direct evanescent coupling to the stabilizing frame is not expected to have played a determining role in the recorded Q-factors.

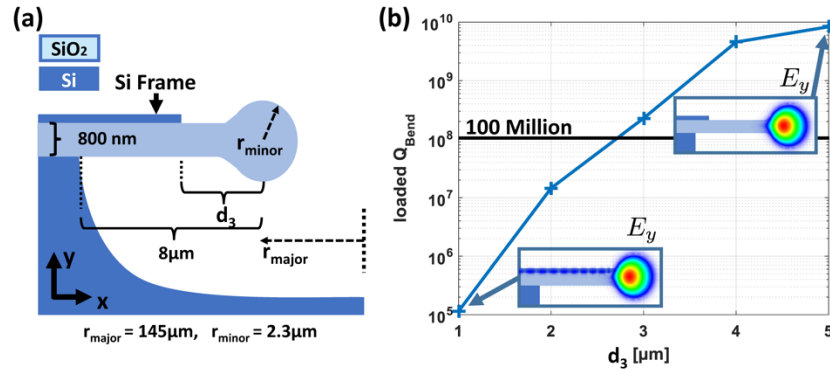


Fig. 15. FEM simulations of the loaded quality factor as limited by bending losses and evanescent losses to the stabilizing frame as a function of the distance  $d_3$  between the toroid center and the edge of the frame. (a) Schematic of the simulation setup. (b) Graph of the loaded quality factor as a function of the distance to the frame. Simulations are indicating that a distance above  $3\ \mu\text{m}$  is sufficient to provide a loaded quality factor of about 100 million, so that the simulated loss channels should then become negligible compared to excess coupler losses and fabrication related losses.

### 5.3. Experimental characterization of the waveguide coupled microtoroids

A critical property of the microtoroid that can lead to a degradation of the intrinsic quality factor [31] and is directly accessible to characterization is its surface roughness after  $\text{CO}_2$  laser reflow. In principle, the reflow process generates an atomically smooth surface. However, it has been reported that evaporation of silica can lead to redeposition, which leads to surface defects that act as additional sources for scattering [34]. An Atomic Force Microscope (AFM) was used to measure the surface roughness, revealing a low roughness root mean square (rms) of  $R_q = 0.45\ \text{nm}$  in the region that was reflowed and a higher roughness on the order of a few nanometers in the rest of the  $\text{SiO}_2$  film (not surprisingly since this surface had been exposed to the silicon device layer patterning ICPRIE etch). Since the mode is pushed towards the silica film at the periphery of the microtoroid core, scattering from the residual roughness is expected to play more of a role here than in the common non-inverted microtoroid geometry.

The initial design of the proposed device was based on a straight coupler design without a stabilizing frame [Fig. 9(a)]. Figure 16(a) shows a raw data transmission spectrum of a straight TM-coupled microtoroid without the stabilizing frame at a temperature setpoint of  $25\ ^\circ\text{C}$ . The spectrum after background normalization and the fitted resonances are shown in Fig. 16(b). Exemplarily, the inset of Fig. 16(b) shows one fitted resonance in zoomed view. This microtoroid has a major radius  $r_{\text{major}} = 147\ \mu\text{m}$ , a minor radius  $r_{\text{minor}} = 2.2\ \mu\text{m}$  (calculated based on Eq. (1)), and a toroid-to-waveguide gap of approximately  $2.4\ \mu\text{m}$  ( $\pm 300\ \text{nm}$ ) which

was measured with the help of an optical microscope. The width of the tapered waveguide in the coupling section is 120 nm.

In order to verify that the recorded resonances are indeed from the microtoroid, further measurements were performed at different temperatures and the shifts in FSR recorded. The group indices  $n_g$  were extracted from the FSR. Figure 17(a) shows the extracted group index  $n_g$  at three different temperatures (25 °C, 45 °C, and 55 °C) and Fig. 17(b) shows the dependency of  $n_g$  on temperature, both in the wavelength range between 1565 nm to 1600 nm. Both the extracted group index and the extracted thermo-optic coefficient confirm that the resonances correspond to light circulating in SiO<sub>2</sub>. While the extracted thermo-optic coefficient is about a factor 2 above the textbook value for SiO<sub>2</sub> [36], confinement effects and thermally induced mechanical deformation, as arising from the thermal coefficient of expansion of the underlying silicon substrate, might also play a role. At  $2.6 \cdot 10^{-6} \text{ K}^{-1}$ , silicon's coefficient of expansion is almost an order of magnitude larger than that of SiO<sub>2</sub>, potentially creating substantial amounts of strain in the inverted microtoroid as the temperature is cycled, as opposed to conventional microtoroids that are less mechanically constrained by anchoring to the silicon pedestal. Moreover, the extracted thermo-optic coefficient is a full order of magnitude too low to correspond to high confinement Si interconnect waveguides, as present elsewhere on the chip.

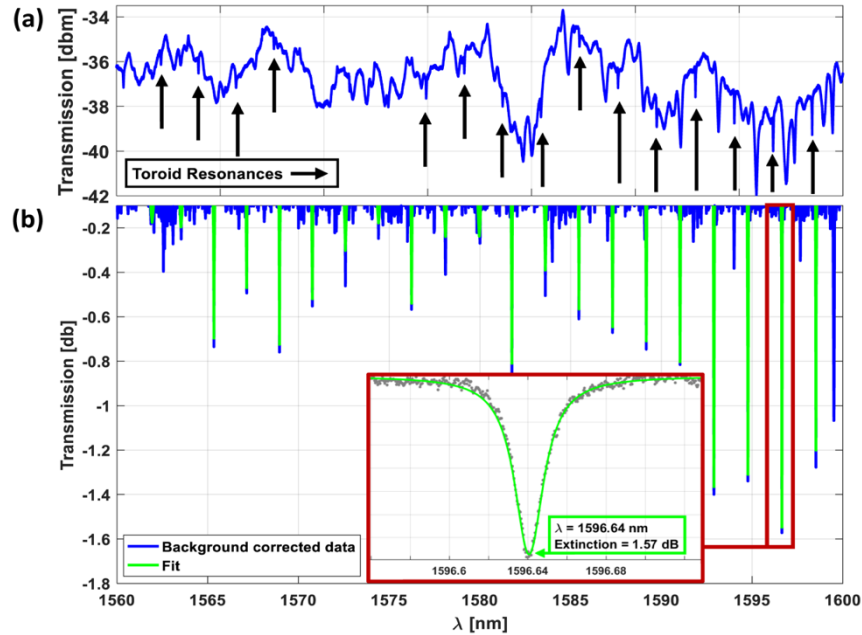


Fig. 16. Transmission spectrum of an inverted silica microtoroid without stabilizing frame coupled to a straight Si waveguide at a temperature setpoint of 25 °C. (a) Raw data transmission spectrum (blue) as a function of wavelength  $\lambda_0$ . The black arrows are indicating the positions of the high-Q resonances of interest. (b) Background corrected spectrum (blue) and fitted resonances (green). The inset shows a detailed view of a representative resonance.

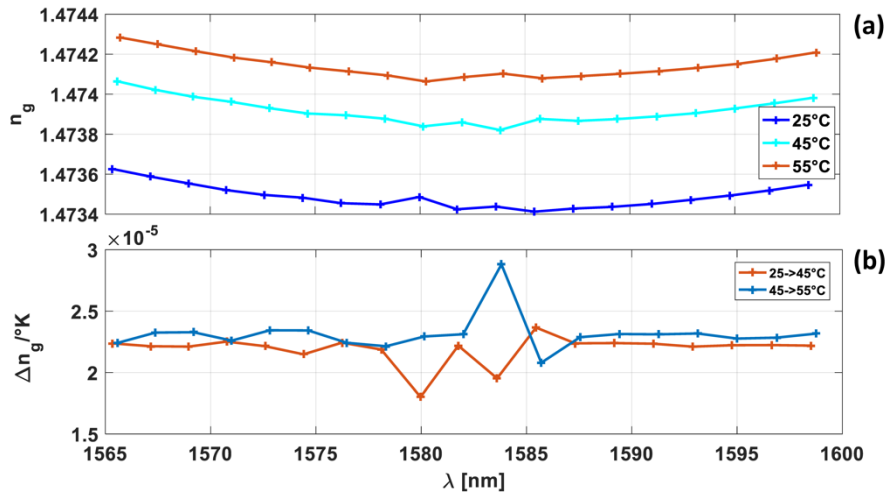


Fig. 17. (a) Group index  $n_g$  of the inverted silica microtoroid coupled to a straight waveguide as a function of wavelength and temperature. (b) Temperature dependence of the group index  $n_g$  as a function of wavelength  $\lambda_0$ .

Further, the intrinsic quality factor  $Q_U$  and the coupling quality factor  $Q_C$  can be extracted by analyzing the measured transmission spectrum of each resonance and fitting the internal resonator loss  $\alpha L + \gamma$ , the coupling loss  $|\kappa|^2 = 1 - |t|^2$  and the group index  $n_g$  [37].  $Q_U$  corresponds to the Q-factor as limited only by internal losses and excess coupler losses (the intrinsic Q-factor in the absence of excess coupler losses), while  $Q_C$  corresponds to the Q-factor as limited only by the coupling losses at the junction. Figures 18(a) and 18(b) are showing the quality factors as a function of wavelength  $\lambda_0$  and temperature.

While  $Q_U$  and  $Q_C$  can both be extracted from a fit of the spectra, they are interchangeable in the fits and cannot generally be distinguished from each other unless it is known whether the resonator is under- or overcoupled. It can be seen in Fig. 18 that the Q-factor identified as  $Q_U$  has a low sensitivity on wavelength, as is expected from the intrinsic Q-factor, while the Q-factor identified as  $Q_C$  is highly dependent on wavelength, as is also expected from the coupling strength. Interestingly, the coupling strength goes down ( $Q_C$  goes up) as the wavelength is increased. While this may appear contra-intuitive at first, as longer evanescent fields at longer wavelengths are usually expected to lead to higher coupling strengths in phase matched directional couplers, here the coupling strength is expected to be limited by phase mismatch, with phase matching improving at shorter wavelengths (since the device was designed to feature phase matching at 1550 nm). Comparison with simulations show the same trend in coupling strengths, even though one would have to assume a slightly larger gap of 2.9  $\mu\text{m}$  to get the exact same coupling strengths (i.e., the device is not quite as overcoupled as one would first assume from modeling). Lower than expected coupling strengths could also be explained e.g. if resonances correspond to the  $\text{TM}_{01}$  instead of the  $\text{TM}_{00}$  mode, however the magnitude of the aforementioned discrepancy is in range of the uncertainty on gap size and exact microtoroid shape. Cleaving the chips through specific microtoroids proved difficult, so that the cross-sections of measured devices could not be imaged one-to-one. Also, further experiments as described below [see also Fig. 19] give additional confirmation that our fabricated devices are in the heavily overcoupled regime.

The extracted coupling Q-factor  $Q_C$  is fifteen to thirty times lower than the intrinsic quality factor  $Q_U$ . Thus, the microtoroid is very highly overcoupled. The intrinsic quality factor  $Q_U$  is found to be on the order of 1.5 million.



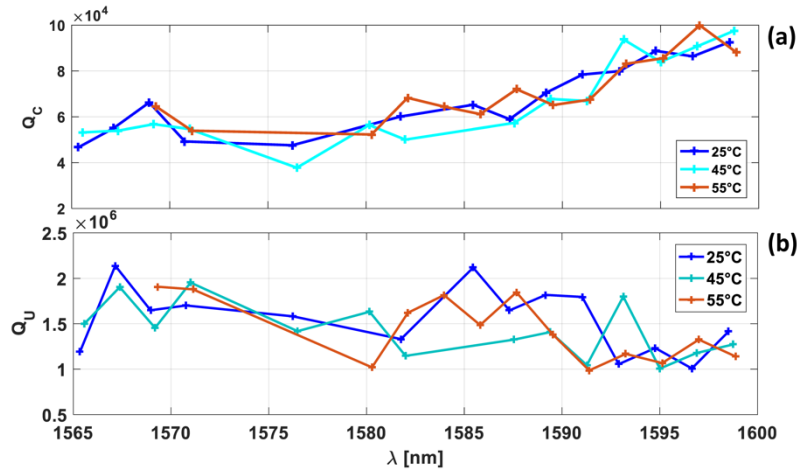


Fig. 18. Measured quality factors  $Q_C$  (a) and  $Q_U$  (b) of the inverted silica microtoroid coupled to a straight waveguide for different temperatures (25 °C, 45 °C and 55 °C) as a function of wavelength  $\lambda_0$ . The intrinsic quality factor  $Q_U$  is found to be on the order of 1.5 million.

Characterization results for a second microtoroid based on the weakly tapered gap junction design and a stabilizing frame are reported in the following (Figs. 9(b) and 10(b)). The second microtoroid has a major radius  $r_{major} = 140 \mu\text{m}$ , a minor radius  $r_{minor} = 2.3 \mu\text{m}$  (calculated based on Eq. (1)), and a toroid-to-waveguide gap (center-to-center) between 3.0 and 3.4  $\mu\text{m}$  as measured with the help of an optical microscope. The width of the tapered waveguide in the coupling section was targeted to be 140 nm and the distance from the waveguide to the edge of the stabilizing frame is 4.8  $\mu\text{m}$ . For providing weak tapering, the bend radius of the coupling section is 1.2 times the targeted major toroid radius. The stabilizing frame has a width of 10  $\mu\text{m}$  and has an overlap with the undercut region of 2  $\mu\text{m}$ .

After the initial reflow step, the microtoroid resonator featured an intrinsic Q-factor on the order of 400,000, actually smaller than for the microtoroid with the straight waveguide. While the stabilizing frame is too far removed from the microtoroid to directly impact its Q-factor via evanescent coupling losses based on the simulation data shown in Fig. 15, it is possible that it indirectly impacts the Q-factor due to process related interactions: Proximity effects during the Si device layer patterning step may result in more surface roughness being transferred to the  $\text{SiO}_2$  film at the bottom of the etch or to more etching reactants being (re)deposited. It is also possible that the simulations shown in Fig. 15 are not fully accurate, as very small losses are notoriously difficult to model, or that the defects in the microtoroid formation associated to the opening of the stabilizing frame (see inset of Fig. 10(b)) remained sufficiently large to spoil the Q-factor.

After initial characterization of the device, a second reflow step was applied to it in an effort to unambiguously distinguish the intrinsic and coupling Q-factors from each other. A part of the microtoroid about 200  $\mu\text{m}$  away from the coupling section was locally reflowed a second time without impacting the coupling section. The  $\text{CO}_2$  laser's beam size and the optical power were decreased for that purpose. Figure 19(a) shows the transmission spectrum after the second reflow step and Fig. 19(b) shows a comparison of the transmission spectra before and after the second reflow step for an individual resonance. It can be seen that not only is the resonance shifted as a consequence of the deformation, the extinction of the resonance is also significantly increased, indicating a coupling regime closer to critical coupling.

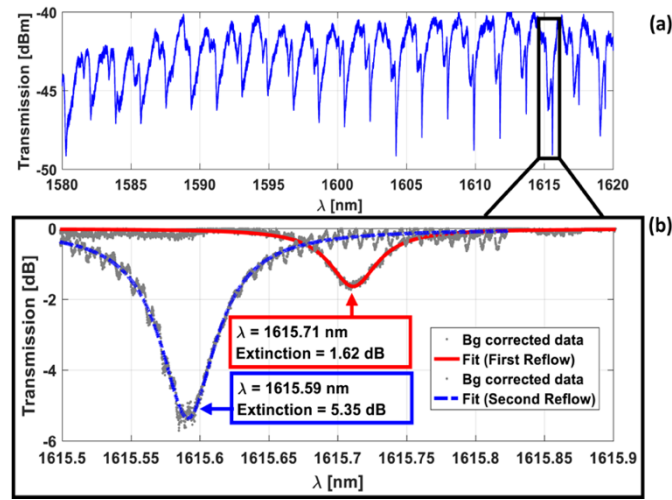


Fig. 19. (a) Transmission spectrum of the inverted silica microtoroid with weakly tapered gap coupler and stabilizing frame after the second local reflow. (b) Direct comparison of a selected resonance before and after the second local reflow. The background corrected data after the first reflow is fitted with a resonance at  $\lambda_{res} = 1615.71$  nm with an extinction of 1.62 dB (solid red). The background corrected data after the second local reflow is fitted with a resonance at  $\lambda_{res} = 1615.59$  nm with an extinction of 5.35 dB.

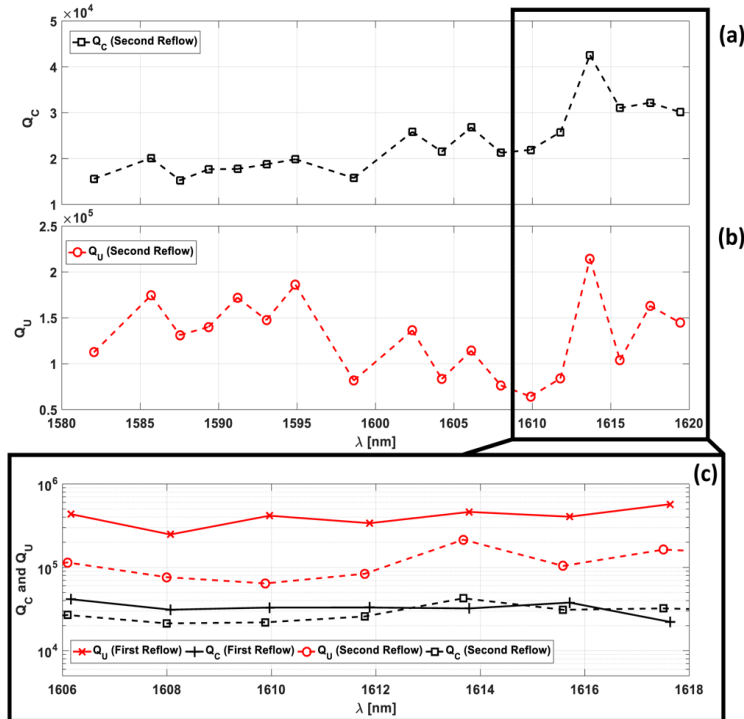


Fig. 20. Semi-logarithmic plot of the intrinsic ( $Q_i$ ) and coupling ( $Q_c$ ) Q-factors of the inverted silica microtoroid with weakly tapered gap coupler and stabilizing frame after the first and the second reflow as a function of wavelength  $\lambda_0$ . (a) shows the data after the second reflow across a wide wavelength range while (b) shows a comparison of the data before and after the second reflow in a restricted wavelength range. The quality-factors could not be reliably extracted over the entire wavelength range prior to the second reflow due to insufficient extinction.

Figures 20(a) and 20(b) show  $Q_C$  and  $Q_U$  as extracted from the transmission spectra before and after the second reflow. Here, the attribution between  $Q_C$  and  $Q_U$  was made based on the expectation of the coupling quality factor not to be impacted by the second reflow step, as it was only applied to a region of the microtoroid remote from the coupling region. One can see that the second reflow step reduced the intrinsic Q-factor to 100,000 – 200,000. This reduction is expected as this highly localized reflow step locally deformed the microtoroid. Given the microtoroid-to-waveguide gap on the order of 3.0  $\mu\text{m}$  to 3.4  $\mu\text{m}$  (as determined from a microscope image), one would have expected a coupling Q-factor  $Q_C$  in the range of 100,000 to 460,000 at  $\lambda_0 = 1600$  nm, which is significantly higher than the 40,000 extracted from the experimental data. Thus, it appears that simulation or process biases have led to higher coupling strengths than initially targeted (a slight reduction in gap to 2.9  $\mu\text{m}$  combined with a slight change in effective index / waveguide width would for example be sufficient to obtain consistency in simulations). While the intrinsic Q-factors that have been obtained with this second structure are not as high as expected for reflowed silica structures, it has the merit of providing additional confirmation that we are generally in the overcoupled regime.

Interestingly, two families of modes can be clearly distinguished in Fig. 19(a), the higher-Q modes already analyzed above, as well as a lower-Q mode family. Based on the observed FSRs, the lower-Q modes have a group index that is slightly higher, by about 0.026, from that of the higher-Q modes. This points the lower-Q modes to have either an x- or y-mode number incremented by one relative to the higher-Q modes. E.g., assuming the higher-Q modes of this microtoroid to be  $\text{TM}_{00}$  and the lower-Q modes to be either  $\text{TM}_{10}$  or  $\text{TM}_{01}$ , the simulated group index differences would be relatively close to the experimentally observed ones, respectively 0.019 and 0.03. Due to the low effective index difference between the  $\text{TM}_{00}$  and the next higher  $\text{TM}_{10}$  /  $\text{TM}_{01}$  modes, on the order of 0.04, it is difficult to rely on phase matching alone for selective mode excitation. On the other hand, getting closer to critical coupling for the targeted high-Q modes would also greatly improve their selective excitation.

It should also be noted that the coexistence of two spectrally overlapping families of modes can skew the data analysis and the extracted Q-factors when simple Lorentzian line shapes are assumed, as here. For example, in the wavelength region around 1595 nm in Fig. 19(a), it can be seen that the recorded high-Q resonances take the shape of Fano resonances as a result of the interference. However, in the wavelength region analyzed in more details in Fig. 20(b) (1606 nm – 1618 nm), the high-Q resonances are sufficiently tuned out of the low-Q ones for Lorentzian line shapes to be recovered. While some remaining skew might remain, this is expected not to be a problem for the data analysis of the first, higher-Q microtoroid, as there the different families of resonances were not overlapping.

There are a number of reasons that could explain why the Q-factors obtained with the integrated structures reported in this paper fall significantly below those obtained with standalone (non-waveguide coupled, non-inverted) microtoroids. Residual scattering losses may be associated to part of the microtoroid mode extending towards the rougher area of the non-reflowed (or only partially reflowed) silica film. The more complex processing associated to waveguide definition might result in reactant (re)deposition that could not have been completely removed during the process flow, improvement of which would require further process development. Simulations might also not be entirely accurate since they rely on Perfectly Matched Layers (PML) acting as absorbing boundary conditions, which can be problematic when extremely small losses are being modeled.

One possible cause may however also be excess coupling losses that could not be independently extracted from the characterization data. Strikingly, for the 140  $\mu\text{m}$  major radius typical for our devices, excess junction losses of 0.1% (i.e., lost power 30 dB below the transmitted power) would be sufficient to spoil the Q-factor to  $\sim 1$  million and explain the experimental data for the first device (straight waveguide coupler). Since the device is very highly overcoupled (15 to 30 times), there would be a very good chance to see substantial improvement of the excess coupling losses if the microtoroid-to-waveguide gap were to be

increased to yield the required coupling strength for critical coupling. It should be noted that excess losses of this magnitude were too low to reliably extract from the 3D FDTD simulations we used to model the junctions. The number of 0.1% thus is only exemplary and serves to illustrate that, at the relatively high intrinsic Q-factors recorded here, very small excess losses are already sufficient to significantly spoil the Q-factor. Finally, while the extracted coupling strengths are roughly consistent with the ones expected from simulations, with discrepancies in range of the expected imprecisions of the modeled geometries, making it plausible for the recorded resonances to correspond to  $TM_{00}$  modes, it is also possible that higher order, lower-Q modes are building up due to the excessive coupling strengths.

While we have so far only shown integration of the microtoroid resonator with a Si interconnect waveguide, the device and process flow was conceived to be in principle compatible with monolithic integration with on-chip electro-optic devices. One remaining issue would then be the deprocessing of the Back-End-Of-Line (BEOL) dielectric layers in the immediate vicinity of the microtoroid prior to microtoroid fabrication out of high quality BOX oxide. The sides of a Si rib waveguide could for example form an etch stop for local BEOL removal, after which the Si slabs on the sides of the waveguide could also be locally removed. Details of the envisioned process flows can be found in [38].

Conventional SiP platforms typically rely on TE polarization, since it is much more straightforward to design and fabricate grating couplers for the latter. Adapting the inverted microtoroid devices described here to using the TE polarization is possible, but also leads to higher bending losses for given BOX layer thickness and microtoroid radius, further constraining the maximum allowable BOX thickness as shown in Fig. 4(a). Alternatively, one may rely on edge couplers, as in this work, with typically better insertion losses and lower polarization dependent losses than in grating coupled platforms. Finally, it is also possible to grating couple TE polarized light onto the chip and rotate the polarization after coupling. A number of device configurations have been developed to achieve the latter in high index contrast waveguide platforms such as SiP [39,40].

As a further integration approach one could also replace the silicon waveguides used here by silicon nitride waveguides, such as for example in [25]. This would have a number of advantages such as allowing to maintain a chosen coupling strength over a much larger temperature range due to a lower thermo-optic coefficient, as well as over a larger wavelength range due to a lower waveguide dispersion, i.e., lower geometric dispersion as a result of the reduced index contrast as well as reduced material dispersion. Moreover, due to the reduced index contrast, the waveguide cross-section could be increased while maintaining the same degree of mode delocalization in the coupling section, relaxing the required critical dimension of the lithography and facilitating the use of Deep Ultra-Violet (DUV) lithography. Here, EBL had to be used due to the unavailability of suitable steppers for sub-100-nm lithography in the chosen academic cleanroom facility. Finally, the reduced index of SiN might also reduce excess coupler losses resulting from scattering. As a disadvantage, however, utilization of SiN waveguides in the microtoroid coupling section would result in the need of one more waveguide transition to silicon based waveguides with electro-optic functionality [24], which is why we opted for direct coupling to silicon waveguides here.

The outstanding issue that remains to be solved here to demonstrate higher-Q devices closer to critical coupling is to increase the microtoroid to waveguide distance. The distance between the microtoroid and the edge of the undercut is constrained by the self-limiting dynamics of the reflow process and are difficult to adjust with timing alone. Changing the laser power or sculpting the  $CO_2$  laser beam profile both provide degrees of freedom, however the highly nonlinear nature of the melting process (arising from the thermal runoff described above) also needs to be taken into account. This being said, it is visible in Figs. 9(a) and 9(b) that a substantial distance remains between the waveguides and the edge of the undercut region ( $> 5 \mu m$ ) in either junction. The waveguides could be repositioned within that

range with only minimal impact on the reflow process. Thus, an additional fabrication campaign should be conducive in improving these devices.

## 6. Conclusions

In conclusion, we have demonstrated a new type of reflowed microtoroid type silica resonator with an inverted topology that is monolithically coupled to a silicon waveguide, as part of a monolithic silicon PIC. Intrinsic quality factors of up to 2 million have been achieved and may be improved upon by further process development. Future work will also involve combining this device with electro-optic components, monolithic integration of which will entail a means to locally deprocess the BEOL prior to microtoroid fabrication.

## Funding

European Research Council (ERC) project “Frontiers of Integrated Silicon Nanophotonics in Telecommunications” (279770); Excellence Initiative of the German Federal and State Governments.

## Acknowledgements

The authors would like to thank Mike Prämassing for taking AFM measurements.

## References

1. P. Del’Haye, A. Schliesser, O. Arcizet, T. Wilken, R. Holzwarth, and T. J. Kippenberg, “Optical frequency comb generation from a monolithic microresonator,” *Nature* **450**(7173), 1214–1217 (2007).
2. P. Del’Haye, T. Herr, E. Gavartin, M. L. Gorodetsky, R. Holzwarth, and T. J. Kippenberg, “Octave spanning tunable frequency comb from a microresonator,” *Phys. Rev. Lett.* **107**(6), 063901 (2011).
3. J. Pfeifle, V. Brasch, M. Laueremann, Y. Yu, D. Wegner, T. Herr, K. Hartinger, P. Schindler, J. Li, D. Hillerkuss, R. Schmogrow, C. Weimann, R. Holzwarth, W. Freude, J. Leuthold, T. J. Kippenberg, and C. Koos, “Coherent terabit communications with microresonator Kerr frequency combs,” *Nat. Photonics* **8**(5), 375–380 (2014).
4. I. Coddington, W. Swann, and N. Newbury, “Coherent dual-comb spectroscopy at high signal-to-noise ratio,” *Phys. Rev. A* **82**(4), 043817 (2010).
5. A. M. Zolot, F. R. Giorgetta, E. Baumann, J. W. Nicholson, W. C. Swann, I. Coddington, and N. R. Newbury, “Direct-comb molecular spectroscopy with accurate, resolved comb teeth over 43 THz,” *Opt. Lett.* **37**(4), 638–640 (2012).
6. F. Dell’Olio, T. Tatoli, C. Ciminelli, and M. N. Armenise, “Recent advances in miniaturized optical gyroscopes,” *J. Eur. Opt. Soc. Rapid Publ.* **9**, 14013 (2014).
7. M. Iqbal, M. A. Gleeson, B. Spaugh, F. Tybor, W. G. Gunn, M. Hochberg, T. Baehr-Jones, R. C. Bailey, and L. C. Gunn, “Label-free biosensor arrays based on silicon ring resonators and high-speed optical scanning instrumentation,” *IEEE J. Sel. Top. Quant. Electron.* **16**(3), 654–661 (2010).
8. J. Witzens and M. Hochberg, “Optical detection of target molecule induced aggregation of nanoparticles by means of high-Q resonators,” *Opt. Express* **19**(8), 7034–7061 (2011).
9. Y. Zhao, Q. Wang, F. Meng, Y. Lin, S. Wang, Y. Li, B. Lin, S. Cao, J. Cao, Z. Fang, T. Li, and E. Zang, “High-finesse cavity external optical feedback DFB laser with hertz relative linewidth,” *Opt. Lett.* **37**(22), 4729–4731 (2012).
10. W. Lewoczko-Adamczyk, C. Pyrlik, J. Häger, S. Schwertfeger, A. Wicht, A. Peters, G. Erbert, and G. Tränkle, “Ultra-narrow linewidth DFB-laser with optical feedback from a monolithic confocal Fabry-Perot cavity,” *Opt. Express* **23**(8), 9705–9709 (2015).
11. W. Yoshiki, Y. Honda, T. Tetsumoto, K. Furusawa, N. Sekine, and T. Tanabe, “All-optical tunable buffering with coupled ultra-high Q whispering gallery mode microcavities,” *Sci. Rep.* **7**(1), 10688 (2017).
12. K. Wörhoff, R. G. Heideman, A. Leinse, and M. Hoekman, “TriPleX: a versatile dielectric photonic platform,” *Adv. Opt. Technol.* **4**(2), 189–207 (2015).
13. A. Coillet, R. Henriet, K. Phan Huy, M. Jacquot, L. Furfaro, I. Balakireva, L. Larger, and Y. K. Chembo, “Microwave photonics systems based on whispering-gallery-mode resonators,” *J. Vis. Exp.* **78**(78), e50423 (2013).
14. I. S. Grudinin, N. Yu, and L. Maleki, “Generation of optical frequency combs with a CaF<sub>2</sub> resonator,” *Opt. Lett.* **34**(7), 878–880 (2009).
15. D. K. Armani, T. J. Kippenberg, S. M. Spillane, and K. J. Vahala, “Ultra-high-Q toroid microcavity on a chip,” *Nature* **421**(6926), 925–928 (2003).
16. X. Zhang and A. M. Armani, “Silica microtoroid resonator sensor with monolithically integrated waveguides,” *Opt. Express* **21**(20), 23592–23603 (2013).
17. J. Yao, D. Leuenberger, M.-C. M. Lee, and M. C. Wu, “Silicon microtoroidal resonators with integrated MEMS tunable coupler,” *IEEE J. Sel. Top. Quant. Electron.* **13**(2), 202–208 (2007).



18. M. Soltani, S. Yegnanarayanan, and A. Adibi, "Ultra-high Q planar silicon microdisk resonators for chip-scale silicon photonics," *Opt. Express* **15**(8), 4694–4704 (2007).
19. J. S. Levy, A. Gondarenko, M. A. Foster, A. C. Turner-Foster, A. L. Gaeta, and M. Lipson, "CMOS-compatible multiple-wavelength oscillator for on-chip optical interconnects," *Nat. Photonics* **4**(1), 37–40 (2010).
20. L. Razzari, D. Duchesne, M. Ferrera, R. Morandotti, S. Chu, B. E. Little, and D. J. Moss, "CMOS-compatible integrated optical hyper-parametric oscillator," *Nat. Photonics* **4**(1), 41–45 (2010).
21. M. H. P. Pfeiffer, A. Kordts, V. Brasch, M. Zervas, M. Geiselmann, J. D. Jost, and T. J. Kippenberg, "Photonic damascene process for integrated high-Q microresonator based nonlinear photonics," *Optica* **3**(1), 20–25 (2016).
22. D. T. Spencer, J. F. Bauters, M. J. R. Heck, and J. E. Bowers, "Integrated waveguide coupled Si<sub>3</sub>N<sub>4</sub> resonators in the ultrahigh-Q regime," *Optica* **1**(3), 153–157 (2014).
23. X. Ji, F. A. S. Barbosa, S. P. Roberts, A. Dutt, J. Cardenas, Y. Okawachi, A. Bryant, A. L. Gaeta, and M. Lipson, "Ultra-low-loss on-chip resonators with sub-milliwatt parametric oscillation threshold," *Optica* **4**(6), 619–624 (2017).
24. W. D. Sacher, Y. Huang, G.-Q. Lo, and J. K. S. Poon, "Multilayer silicon nitride-on-silicon integrated photonic platforms and devices," *J. Lightwave Technol.* **33**(4), 901–910 (2015).
25. K. Y. Yang, D. Y. Oh, S. H. Lee, Q.-F. Yang, X. Yi, B. Shen, H. Wang, and K. Vahala, "Bridging ultrahigh-Q devices and photonic circuits," *Nat. Photonics* **12**(5), 297–302 (2018).
26. P. Dumon, W. Bogaerts, V. Wiaux, J. Wouters, S. Beckx, J. Van Campenhout, D. Taillaert, B. Luyssaert, P. Bienstman, D. Van Thourhout, and R. Baets, "Low-loss SOI photonic wires and ring resonators fabricated with deep UV lithography," *IEEE Photonics Technol. Lett.* **16**(5), 1328–1330 (2004).
27. A. K. Paul, A. K. Dimri, and R. P. Bajpai, "Plasma etch models based on different plasma chemistry for micro-electro-mechanical-systems application," *Vacuum* **68**(2), 191–196 (2002).
28. M. Sheik-Bahae and H. S. Kwok, "Controlled CO<sub>2</sub> laser melting of silicon," *J. Appl. Phys.* **63**(2), 518–524 (1988).
29. A. D. McLachlan and F. P. Meyer, "Temperature dependence of the extinction coefficient of fused silica for CO<sub>2</sub> laser wavelengths," *Appl. Opt.* **26**(9), 1728–1731 (1987).
30. T. J. Kippenberg, S. M. Spillane, D. K. Armani, and K. J. Vahala, "Fabrication and coupling to planar high-Q silica disk microcavities," *Appl. Phys. Lett.* **83**(4), 797–799 (2003).
31. A. Schließer, *Cavity Optomechanics and Optical Frequency Comb Generation with Silica Whispering-Gallery-Mode Microresonators* (Dissertation, LMU München, 2009).
32. M. Pu, L. Liu, H. Ou, K. Yvind, and J. M. Hvam, "Ultra-low-loss inverted taper coupler for silicon-on-insulator ridge waveguide," *Opt. Commun.* **283**(19), 3678–3682 (2010).
33. C. Kopp, S. Barnabé, B. Ben Bakir, J.-M. Fedeli, R. Orobtcouk, F. Schrank, H. Porte, L. Zimmermann, and T. Tekin, "Silicon photonic circuits: On-CMOS integration, Fiber optical coupling, and packaging," *IEEE J. Sel. Top. Quant. Electron.* **17**(3), 498–509 (2011).
34. T. J. Kippenberg, *Nonlinear Optics in Ultra-high-Q Whispering-Gallery Optical Microcavities* (Dissertation, California Institute of Technology, 2004).
35. J. Richter, M. P. Nezhad, and J. Witzens, "Monolithically integrated waveguide-coupled silica microtoroids," in *Proc. 2015 Opto-Electronics and Communications Conference (OECC)*.
36. D. B. Leviton and B. J. Frey, "Temperature-dependent absolute refractive index measurements of synthetic fused silica," arXiv:0805.0091 (2008).
37. D. G. Rabus, *Integrated Ring Resonators* (Springer-Verlag Berlin Heidelberg, 2007), Chap. 2.
38. J. Witzens, "Integrated microtoroids monolithically coupled with integrated waveguides," US Patent 9268086B2 filed Aug. 2013.
39. D. Dai and J. E. Bowers, "Novel concept for ultracompact polarization splitter-rotator based on silicon nanowires," *Opt. Express* **19**(11), 10940–10949 (2011).
40. Y. Xiong, D.-X. Xu, J. H. Schmid, P. Cheben, S. Janz, and W. N. Ye, "Robust silicon waveguide polarization rotator with an amorphous silicon overlayer," *Photon. J.* **6**(2), 2200308 (2014).